Optimization of Long-Range Order in Solvent Vapor Annealed Poly(styrene)-*block*-poly(lactide) Thin Films for Nanolithography

A. Baruth,[†] Myungeun Seo,[‡] Chun Hao Lin, Kern Walster, Arjun Shankar, Marc A. Hillmyer,* and C. Leighton*

Department of Chemical Engineering and Materials Science and Department of Chemistry, University of Minnesota, Minneapolis, Minnesota 55455-0431, United States

Ⓢ *Supporting Information*

ABSTRACT: Detailed experiments designed to optimize and understand the solvent vapor annealing of cylinder-forming poly(styrene)-*block*-poly(lactide) thin films for nanolithographic applications are reported. By combining climate-controlled solvent vapor annealing (including in situ probes of solvent concentration) with comparative small-angle X-ray scattering studies of solvent-swollen bulk polymers of identical composition, it is concluded that a narrow window of optimal solvent concentration occurs just on the ordered side of the order−disorder transition. In this window, the lateral correlation length of the hexagonally close-packed ordering, the defect density, and the cylinder orientation are simultaneously optimized, resulting in single-crystal-like ordering over 10 μm scales. The influences of polymer synthesis method, composition, molar mass, solvent vapor pressure, evaporation rate, and film thickness have all been assessed, confirming the generality of this behavior. Analogies to thermal annealing of elemental solids, in combination with an understanding of the effects of process parameters on annealing conditions, enable qualitative understanding of many of the key results and underscore the likely generality of the main conclusions. Pattern transfer via a Damascene-type approach verified the applicability for high-fidelity nanolithography, yielding large-area metal nanodot arrays with center-to-center spacing of 38 nm (diameter 19 nm). Finally, the predictive power of our findings was demonstrated by using small-angle X-ray scattering to predict optimal solvent annealing conditions for poly(styrene)-*block*-poly(lactide) films of low molar mass (18 kg mol^{-1}). High-quality templates with cylinder center-to-center spacing of only 18 nm (diameter of 10 nm) were obtained. These comprehensive results have clear and important implications for optimization of pattern transfer templates and significantly advance the understanding of self-assembly in block copolymer thin films.

KEYWORDS: *block copolymer, solvent vapor annealing, self-assembly, lithography, nanodot array, small-angle X-ray scattering*
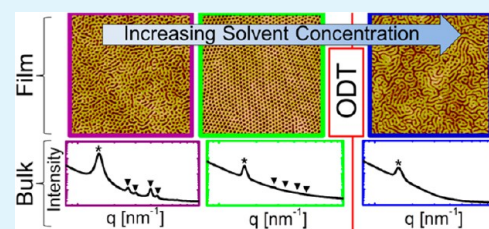
INTRODUCTION

Block copolymer (BCP) self-assembly is of high contemporary interest in thin (∼100 nm) films due to applications in areas traditionally dominated by photo- and electron-beam lithography.[1−9] The large-area self-assembly of lithographic features in such films potentially provides a faster and cheaper alternative to conventional lithography in certain circumstances, and may be possible with feature fidelity comparable to that of conventional lithography[3,10] even at smaller sizes.[7,11,12] In diblock copolymers, including the intensively studied poly-(styrene)-*block*-poly(lactide) (PS-PLA), it is possible to obtain microphase-separated morphologies with natural periodicities in the 10−100 nm range.[13] In terms of fabricating large-area nanodot and nanowire arrays, cylinder-forming compositions are particularly attractive.[3,14] While the bulk self-assembly of cylinder-forming diblock copolymers is relatively well understood, controlling this self-assembly in thin films remains challenging due to issues with both finite size effects and complex phenomena driven by surface and interface energies.[15−18] These factors impact cylinder orientation, lateral ordering, and uniformity, and thus play a key role in setting the ultimate limits of BCP nanolithography.

Spin-cast thin films are the typical starting point for most BCP nanolithography processes. In such kinetically trapped "crystalline" systems, one approach to reducing defect-densities and increasing structural correlation lengths is the use of thermal treatment. This increases the mobility of the crystallizing particles (e.g., atoms, molecules, or, as in the present case, polymer cylinders) facilitating reorganization into thermodynamically favored structures. In some BCP thin films, thermal treatment above the highest glass transition temperature (T_g) of the two polymers is indeed effective in obtaining equilibrium structures with optimized characteristics for lithography.[19,20] An alternative to direct thermal annealing of BCP films is solvent vapor annealing (SVA), where a thin film is exposed to solvent vapors, thus forming a swollen and mobile polymer layer at temperatures well below the highest T_g of the system.[21] This technique was originally introduced as an alternative to thermal annealing for BCPs exhibiting thermal degradation, problematic thermally driven transitions,[22−24] or

slow dynamics due to high molar mass. The interest in SVA of BCPs has grown well beyond this in recent years, however, as it has been shown to have wide potential to promote preferred feature orientation, long-range order, and low defect density. Moreover, time requirements for optimal organization are often significantly shorter for SVA than thermal annealing, due to the chain mobilities that can be obtained.[21]

A major complicating factor in the optimization of SVA for BCP applications, including lithography, is the paucity of established connections between the properties of swollen films (i.e., in the state relevant to SVA) and films in the final dried state. To establish reliable relationships of this type, it is imperative that critical SVA parameters (such as chamber volume, temperature, solvent purity, pressure, and annealing time) are carefully controlled, and that the film structure and properties be appropriately characterized in both the swollen and the final states.[25−28] Even relatively simple AB diblock copolymer systems have rich phase diagrams in the temperature−solvent concentration plane, meaning that control and understanding of the solvent vapor pressure, and the amount of solvent uptake by the film, are critical.[26,29] Early work on bulk BCPs focused on understanding these factors,[26,29] and now new insights, including the prominent role played by solvent vapor pressure and annealing time, are emerging for thin films. For example, the ratio of film/solvent interfacial area to SVA chamber volume (in a slowly leaking vessel) was recently used to parametrize the annealing process for cylinder-forming poly(styrene)-*block*-polydimethylsiloxane BCPs in acetone and chloroform vapor. For fixed swelling and deswelling rates, the time in the swollen state was particularly important in dictating the final BCP film morphology.[30,31]

Recent studies have also highlighted the strong effects of solvent evaporation rate on the final morphology at the free surface of BCP films.[32] When the solvent evaporates from a swollen film, it is thought to either "freeze-in" the organization of the swollen state or cause a directed ordering front to propagate through the bulk of the film.[14] In either case, the consequences of this evaporation-induced transition are dependent on the exact trajectory through the BCP phase diagram as solvent is removed,[25,33] with changes in polymer dynamics, and drying-induced lyotropic transitions, serving as complicating factors. One of the most direct methods used to elucidate these connections is in situ grazing incidence small-angle X-ray scattering (GISAXS). Investigations using GISAXS have focused, for example, on the orientational changes during annealing of cylinder-forming poly(styrene)-*block*-poly(4-vinyl-pyridine) thin films. Chloroform, a nonselective solvent, was found to yield parallel cylinder orientation. Conversely, a selective solvent (1,4-dioxane) gave perpendicular cylinder orientation.[17] In cylinder-forming poly(styrene)-*block*-poly-(ethylene oxide) films, GISAXS was used to probe the solvent evaporation rate dependence, suggesting that fast evaporation leads to the formation of an ordering front that drives perpendicular orientation of cylinders along the solvent gradient.[14] If the evaporation is too rapid, however, BCP films can become kinetically trapped in the dried state, resulting in alternate, often disorganized, morphologies.[34] GISAXS was also recently used to establish correlations between the swelling ratio (i.e., the amount of neutral solvent in the swollen film) and the final film morphology for poly(styrene)-*block*-poly(2-vinylpyridine), producing in-plane cylinders.[35] Additionally, combined theoretical and experimental studies of solvent concentration profiles[36] (and their effects on the orientation

of cylinder-forming BCPs) have suggested that the cylinder growth rate during evaporation is a product of both a thermodynamic driving force and polymer chain relaxations. In the case where the relaxation time increases more rapidly with depth than the driving force decreases (i.e., the fast evaporation regime), the cylinders were found likely to orient perpendicular to the film surface.[18,37]

On the basis of these (and other) recently published developments, and practices developed empirically over a substantial period of time in our research, a number of important themes emerge in terms of enhancing reliability and reproducibility of SVA for highly ordered BCP films. First, it is now clear that selectivity of the solvent vapor can be used to manipulate the free surface energy, thus dictating the preferred orientation of the self-assembled features. This can be accomplished by creating an effectively neutral free surface, or a surface that is preferential for one block.[21,38,39] For example, to encourage perpendicular cylinder orientation in PS-PLA, the essentially neutral solvent THF is necessary.[39] Second, it is also becoming clear that the presence of even small concentrations of water in the SVA process can be particularly important, as its polar nature leads to high selectivity toward the more hydrophilic blocks.[39] In some BCP systems containing a hydrophilic poly(ethylene oxide) block, the presence of water vapor has been shown critically important, and even useful.[40,41] For PS-PLA, on the other hand, the presence of water during SVA detrimentally modifies both the solvent evaporation rate and the surface energy, typically producing a PLA wetting layer at the free surface.[39] Somewhat related to this, it also appears advantageous to work with starting BCP films that contain minimal residual solvents, including water for the PS-PLA case. In general, this can be simply accomplished via mild thermal pretreatment of the films (well below T_g). To fully understand the SVA process, it is thus clearly necessary to control and understand the solvent composition, perhaps to quite exacting levels. Third, on the basis of the recent work of Phillip et al.,[18] it is important to remove the solvent sufficiently fast to induce propagation and growth of the ordered phase perpendicular to the film surface. Finally, a consensus appears to be emerging that in situ control and monitoring of the extent of solvent incorporation in the film during SVA is important. Examining recent literature, for instance, it can be seen that in situ thickness monitoring has become quite standard,[21] although, critically for the current study, a general understanding of the optimum solvent concentration remains elusive.

In this work, we show, by combining the above summarized "best practices" with careful in situ control of film swelling, and comparative small-angle X-ray scattering (SAXS) studies of swollen bulk BCPs of the same composition, that through SVA we can reproducibly achieve highly ordered nanoscopic features in a wide variety of PS-PLA BCPs. Our results provide excellent statistics on a large number of BCP samples (at various molar masses and compositions), with center-to-center cylinder spacing from 43−59 nm. Critically, our investigations address both the evaporation time and the solvent concentration during SVA. In particular, we performed extensive SVA experiments on PS-PLA thin films with in situ thickness monitoring, comparing resulting film microscopy data with SAXS from a parallel series of identical composition bulk PS-PLA samples with various solvent loadings. The combined analyses provide a clear picture of the role of solvent concentration on final morphology in the dried state. We show, for example, that there exists a well-defined window of solvent concentration, just on

the ordered side of the order/disorder transition (ODT) of PS-PLA solutions, which consistently yields optimally ordered perpendicular cylindrical structures with maximized lateral correlation length (up to ~10 μm) and minimized defect density. We further show (i) that such films are of sufficient quality to enable high-fidelity pattern transfer to Ni metal (creating Ni nanodot arrays with a 38.0 ± 0.6 nm center-to-center spacing), and (ii) that SVA annealing of low molar mass PS-PLA thin films can yield well-ordered cylindrical arrays with a center-to-center spacing of only 18 nm and pore diameters down to 10 nm. We also draw firm conclusions on the influence of solvent evaporation rate, and attempt to resolve some apparent discrepancies in the current literature on optimal evaporation rates.

■ METHODS

Synthesis of Poly(styrene)-*block*-poly(lactide). Two separate synthesis routes were used to produce PS-PLA, method 1 and method 2. In method 1, hydroxyl-terminated PS (M_n = 42.5 kDa), previously synthesized via living anionic polymerization, was placed in a drybox. The subsequent PLA was synthesized via ring-opening trans-esterification polymerization (ROTEP) of D,L-lactide using 1,8-diazabicyclo[5.4.0]undec-7-ene (DBU) as a catalyst. The polymerization was conducted in dichloromethane at room temperature for 1 h. After termination with benzoic acid, PS-PLA was obtained by precipitating in methanol. The final PS-PLA had a total M_n = 63 kDa, with a PLA volume fraction of 0.28 (by volume) yielding a cylindrical morphology with a polydispersity index of 1.08. Details on polymer molecular weight, polydispersity, and phase fraction were obtained from proton nuclear magnetic resonance (^{1}H NMR) spectroscopy and size-exclusion chromatography (SEC).

In method 2, PS-PLA was synthesized by a combination of ROTEP and reversible addition—fragmentation chain transfer (RAFT) polymerization. Hydroxyl-terminated PLA was synthesized by polymerizing D,L-lactide using AlEt$_3$ as a catalyst. S-1-Dodecyl-S′-(R,R′-dimethyl-R″-acetic acid) trithiocarbonate (CTA) then was coupled with PLA to generate PLA-CTA. In a degassed and sealed ampule, styrene was polymerized in bulk at 120 °C (by thermal initiation) in the presence of PLA-CTA to generate PS-PLA. Polymerization time was varied to control the molecular weight of PS. The polymerization mixture was cooled to room temperature, diluted with dicholoromethane, and precipitated in methanol. The polymer was collected by filtration, purified by reprecipitation in methanol, and dried under vacuum. The final PS-PLA polymers had a total range M_n = 18−103 kDa, with a PLA volume fraction of 0.21−0.28 (by volume), all yielding a cylindrical morphology with a molar mass dispersity of 1.10−1.20. Details on polymer molar mass, dispersity, and composition were obtained from ^{1}H NMR spectroscopy and SEC. DSC measurements confirmed a depression of T_g in the presence of THF. For example, bulk neat (i.e., 0% THF volume fraction) PS-PLA with M_n = 103 kg/mol and f_{PLA} = 0.21 (denoted SL (79-24) hereafter, where $M_{n,PS}$ = 79 kg/mol and $M_{n,PLA}$ = 24 kg/mol, where f_{PLA} is the volume fraction of PLA) exhibited two T_g's at 50 and 105 °C corresponding to PLA and PS, respectively. In comparison, bulk SL (79-24) with THF volume fraction Φ_{THF} = 47% solutions exhibited T_g's at −11 and 0 °C for PLA and PS. Furthermore, bulk neat SL (12-6) had T_g's that were much lower, appearing at 23 and 50 °C for PLA and PS. This suggests that the T_g's were sufficiently low for solvent vapor annealing, as discussed below, to occur even in the low molar mass polymer at lower Φ_{THF}.

Thin Film Preparation. Typical solutions of 1.5% (w/v) PS-PLA in toluene were spin coated onto hexamethyldisilazane (HMDS) treated, natively oxidized silicon wafers (20 mm × 20 mm). HMDS treatment of the Si wafers was carried out by ultrasonically cleaning substrates in organic solvents (acetone followed by methanol), treating them in a 1:5 (v/v) HMDS:toluene solution for 16 h, then rinsing in toluene and blowing dry with N$_2$ gas. The films were spin coated at 2000 rpm, diced into ~10 usable pieces (5 mm × 5 mm), and

immediately placed in an 85 °C oven for drying. Samples were dried for a minimum of 1 h and a maximum of 3 days. This process yielded ~60 nm thick films; adjustments to solution concentration and spin speed were made for thicker films. Thin films were subsequently hot-loaded into a purged, overpressured solvent annealing chamber and immediately sealed to avoid any water contamination. Following exposure to solvent vapor (as described below), the samples were immediately transferred to a 0.05 M NaOH solution (H$_2$O:CH$_3$OH = 6:4 by volume) for PLA minority domain degradation. They were then left to soak for 45 min, "locking-in" the final morphology of the film. This was followed by a 10 s O$_2$ reactive ion etch (60 W for 20 s in 30 mTorr) to remove any polymer wetting layer[10,42] at the polymer/HMDS interface and the HMDS itself. Samples at this stage were immediately imaged with atomic force microscopy (AFM), without any further modification. For scanning electron microscopy (SEM), a ~3 nm layer of Pt was coated across the surface for subsequent imaging. For backside imaging, the thin films were placed upside down on double-sided Scotch brand transparent tape and placed in liquid N$_2$. Following liquid N$_2$ exposure, the Si wafer was peeled away from the film providing access to the underside. These films were again exposed to a 20 s O$_2$ reactive ion etch (60 W for 20 s in 30 mTorr) to remove any polymer wetting layer.

Small-Angle X-ray Scattering. As described previously (see ref 46), SAXS samples were prepared in aluminum DSC pans (Tzero hermetic). A controlled amount of polymer was loaded into a pan, and then solvent was added using a micropipette. The amount of solvent was determined by weighing the pan after sealing, and subtracting the mass of (pan + polymer) from the mass of the sealed pan. Polymer samples without solvent were also prepared and annealed in the TA Q20 DSC at 150 °C for 5 h and slowly cooled to room temperature (2 °C/min). SAXS experiments were performed at the Advanced Photon Source at Argonne National Laboratory at the Sector 5-ID-D beamline, having a resolution of Δq = 0.001 nm^{-1}, using a step size of Δq = 0.004 nm^{-1}. The wavelength of the X-rays was 0.73 Å, and the sample to detector distance was 4.6 or 4.0 m. The scattering intensity was monitored by a Mar 165 mm diameter CCD detector with 2048 × 2048 pixels. The two-dimensional scattering patterns were azimuthally integrated to obtain one-dimensional profiles presented as scattered intensity versus scattering vector (q), where the magnitude of the scattering vector is given by $q = (4\pi/\lambda) \sin \theta$, θ being the incident angle. Scattering data were Lorentz corrected,[29,43] and contributions arising from background Porod (q^{-4}) scattering and a constant baseline were considered. The resultant peaks were fit with a Lorentzian, as indicated in Supporting Information Figure S1.

Other Characterization. ^{1}H NMR spectra were obtained on Varian INOVA-300, VXR-300, or INOVA-500 spectrometers in CDCl$_3$ at room temperature. Samples were prepared by dissolving approximately 20 mg of polymer in approximately 0.700 mL of deuterated chloroform. Each spectrum was obtained after 32 scans with a 20 s pulse delay. SEC was performed on an Agilent 1100 series instrument equipped with an HP 1047A refractive index detector. Three PLgel Mixed C columns as well as a PLgel 5 μm guard column from Varian were employed. Chloroform was used as the mobile phase at 35 °C flowing at a rate of 1 mL/min. Polymer samples were prepared at an approximate concentration of 0.3% (wt:wt) in chloroform. Molecular weights were determined from calibrated curves created from narrow molar mass distribution PS standards purchased from Polymer Laboratories. For thin films, the thickness was determined in situ with a Filmetrics F20-UV general-purpose film thickness measurement system with both halogen and deuterium sources. Spectral reflectance data were taken every 100−250 ms, with a 40 ms integration time, and modeled immediately over a spectral range of 270−900 nm for real-time thickness measurements. From the fitted spectra, we were able to develop expected refractive index profiles based on known values (e.g., PS, n = 1.59; PLA, n = 1.482; THF, n = 1.407). Thus, we anticipated an index of refraction of ~1.55 for the neat film, dropping to 1.45 with increasing Φ_{THF}. If this trend in the index of refraction was not observed in the fitting, the SVA run was not considered viable for the study. Tapping mode AFM was performed on a Digital Instruments Nanoscope III microscope using
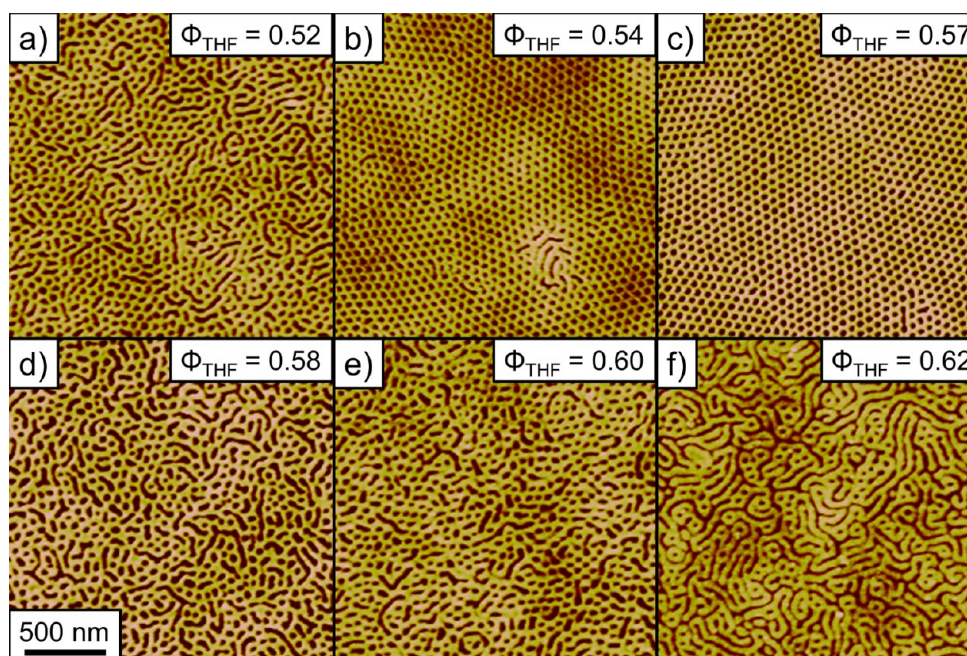
Figure 1. Representative tapping-mode AFM images (after PLA degradation) from ~60 nm thick SL (51−24) films solvent vapor annealed at various Φ_{THF}: (a) 0.52, (b) 0.54, (c) 0.56, (d) 0.58, (e) 0.60, and (f) 0.62. The solvent vapor annealing was performed at low pressure (<1 psig), for 1 s, followed by quenching in <1 s. Each image is 2×2 μm^2 with a height scale of 20 nm.

engagement set points between 0.9−0.95 of the free amplitude oscillation. SEM was performed on films sputter-coated with 3 nm of Pt on a Hitachi S900 FE-SEM using an accelerating voltage between 3.0 and 5.0 kV.

RESULTS

In subsection A, we present the results of studies aimed at optimizing the final BCP film surface morphology with respect to solvent concentration, solvent vapor pressure, and the exact SVA protocol employed. We provide detailed characterization of the thin films through cross-sectional and film/substrate interface observations, and demonstrate high-fidelity lithographic patterning using these templates with Ni metal films, via a Damascence-type approach. In subsection B, we present the results of comparative SAXS studies of bulk PS-PLA specimens (at compositions identical to those studied in film form) as a function of solvent concentration. Together, these results clearly indicate an optimized window of solvent concentration for lithographic applications, lying just on the ordered side of the order−disorder transition. In the Discussion, we demonstrate the extrapolative power of SAXS analysis to successfully predict an optimized SVA window for low molar mass PS-PLA BCPs. Finally, we elucidate the role of solvent evaporation and clarify its relationship to the swollen state of the film.

A. Solvent Vapor Annealing of Thin Films. The SVA process can be susceptible to even apparently minor perturbations in annealing conditions. Through an iterative process, we thus systematically minimized the various sources of these irreproducibilities, resulting in the development of strict annealing protocols, and, ultimately, the climate-controlled SVA chamber shown in Figure S2 and discussed in Supporting Information. This solvent annealing chamber (SAC) is constructed from all-metal components (i.e., the chamber itself, the various valves, the sealing gaskets, etc.) to avoid the possibility of solvent-induced degradation and

subsequent potential contamination. As described elsewhere,[10] the chamber is supplied by a dry N_2 gas line (from liquid N_2 boil-off), which is split into two flow-controlled inlets. Inlet 1 is used to purge the sample space both before annealing and during solvent evaporation (i.e., quenching). Dry N_2 gas purging ensures the lowest possible humidity environment during SVA, while the injection of gas during quenching enables the most controllable and rapid expulsion of the solvent vapor. Inlet 2, however, is passed through a sealed solvent bubbler that delivers molecular-sieve-dried vapor-phase solvent to the sample space at a measured and controlled flow-rate. All vapor thus delivered to the sample space exits through a controlled-flow outlet to enable pressure control inside the chamber.

The SAC also offers direct optical access to the sample through a fused silica viewport, enabling in situ spectral reflectance-based measurements of film thickness. The rate of thickness data acquisition (or equivalently solvent concentration, Φ_{THF}) was typically 5 or more points per second, providing a detailed picture of the film swelling (controlled by inlet and outlet flows) and deswelling process during solvent incorporation and evaporation. Throughout this section, the solvent loading of the sample is given as a volume concentration, Φ_{THF}, and is defined by

$$\Phi_{THF} = \frac{V_{solvent+film} - V_{film}}{V_{solvent+film}}$$

$$= \frac{t_{solvent+film} - t_{film}}{t_{solvent+film}}$$

$$= 1 - \frac{t_{film}}{t_{solvent+film}} \qquad (1)$$

where V denotes volume and t thickness. As supported by direct observation, the areas for the two film states (i.e., swollen and dry) are taken to be nominally identical, and thus only a thickness measurement is required to obtain a real-time in situ

probe of Φ_{THF} during SVA. As shown in more detail in Supporting Information Figure S3, using this in situ measurement of Φ_{THF}, we divide the SVA process into four distinct time regimes. The initial period includes the opening of the solvent bubbler to the SAC, resulting in an abrupt increase in solvent concentration over 20–30 s. The second regime involves the continued uptake of solvent into the film and a gradual increase in thickness over a period of 2–4 min, until the target swelling level is reached. The rate of swelling in this second regime was found to have no obvious impact on the final morphology of the film. The third regime is characterized by a relatively constant solvent concentration, and the anneal time specified for the various experiments is in this regime. In the fourth regime, evaporation of the majority of the solvent (around 90%) occurs in less than 1 s, and the remaining solvent is removed over the next ~5 s.

In all experiments, large (i.e., 20 mm × 20 mm) hydrophobically modified Si wafers were used as substrates for spin-casting PS-PLA BCP films from toluene. The films were then immediately diced into about 10 pieces (~5 mm × 5 mm) and placed in an 85 °C gravity convection oven for at least 1 h prior to SVA. Note that we observed up to an 8% decrease in film thickness after this thermal treatment, implying some initial removal of trapped solvents (likely including water) after spin-casting. Further thickness changes were minimal beyond this period. The samples were then hot-loaded directly from the oven into the N_2 purged SAC (ambient temperature 21 ± 0.5 °C), with a large positive pressure maintained to avoid moisture contamination during transfer.

The results of a representative experiment probing the influence of Φ_{THF} on the final film surface morphology are shown in Figure 1. In this experiment, 60 nm thick PS-PLA films with M_n = 75 kg/mol and f_{PLA} = 0.28 (denoted SL (51-24) hereafter, where $M_{n,PS}$ = 51 kg/mol and $M_{n,PLA}$ = 24 kg/mol), where f_{PLA} is the volume fraction of PLA, were solvent vapor annealed at low solvent vapor pressures (<1 psig). The annealing time (as defined above, i.e., region 3 of Supporting Information Figure S3) was fixed at 1 s (a significantly shorter annealing time than that shown in Supporting Information Figure S3), and the quenching time was less than 1 s. The resulting films were then immediately placed in a 0.05 M NaOH solution (H_2O:CH_3OH = 6:4 by volume) for 45 min to completely remove the PLA minority component.[44] The AFM images as a function of Φ_{THF} in Figure 1 (only Φ_{THF} values from 0.52 to 0.62 are shown) demonstrate remarkable surface morphology changes over a small range of Φ_{THF}. In the narrow window 0.54 ≤ Φ_{THF} ≤ 0.57, a hexagonally packed cylindrical morphology is clearly observed with a center-to-center spacing of 37 ± 0.9 nm, perpendicular orientation, low dispersity in feature size, low areal defect density, and high (of order 1 μm) lateral correlation length. At Φ_{THF} values outside of this window, a mixed morphology, containing both in-plane and perpendicular cylinders, was observed. At low Φ_{THF}, small regions (up to 200 nm across) of perpendicularly oriented cylinders surrounded by parallel cylinders were evident and comparable to an unannealed film. At higher solvent concentrations, a mixed phase was observed, with little evidence of lateral ordering. At the very highest concentrations shown here (i.e., Φ_{THF} = 0.62), the majority of cylinders were found to lie in-plane, with little lateral ordering; this behavior persists at Φ_{THF} > 0.62.

Similar experiments were performed on four PS-PLA polymers (with varying compositions), encompassing two

synthesis methods, three film thicknesses, and both high (>10 psig) and low (<1 psig) solvent exposure pressures. In this series of experiments, the solvent exposure took place over 180 s (i.e., region 3 of Supporting Information Figure S3), and the quench occurred in less than 1 s. Although the effects of annealing time were not extensively investigated, an increase in lateral correlation length in samples annealed for 180 s (Figure 1), cf., 1 s (Figure 2) was observed. Preliminary investigations
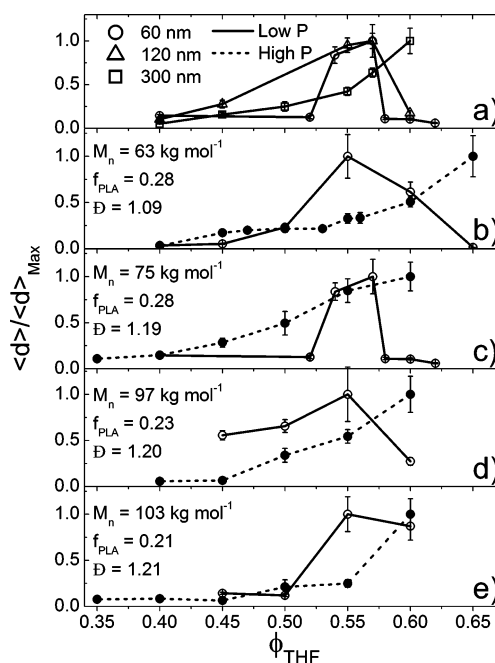

Figure 2. Normalized lateral correlation length (i.e., grain diameter of the cylindrical ordering) as a function of Φ_{THF}, under various conditions. Panel (a) shows results on SL (51−24) for three film thicknesses, 60, 120, and 300 nm. Each anneal was performed for 3 min at low pressure (<1 psig). Panels b−e show normalized diameters for four PS-PLA BCPs, with varying total molar mass, volume fraction of PLA, and dispersion in molar mass, as indicated. Each anneal was performed for 3 min. Open circles with solid lines are 60 nm films exposed to low pressure (<1 psig). Closed circles with dotted lines are 60 nm films exposed to high pressure (in excess of 10 psig). Error bars represent the standard deviation of multiple trials, as discussed in the text.

with longer anneal times (e.g., 15 min or more) did not lead to an obvious increase in correlation length after 3 min. Figure 2 plots the normalized lateral correlation length (i.e., the normalized grain diameter) obtained from SEM images as a function of Φ_{THF}. SEM image analysis, as detailed in Supporting Information Figure S4, was performed for at least three runs (error bars represent the standard deviation) at each experimental condition (i.e., molar mass, thickness, pressure, and synthesis method) to generate the compiled results in Figure 2. In a given series, each experiment was performed on the same day, on a separate piece of the same wafer. Between the various series, however, small variations occurred in parameters such as initial thickness, relative humidity, and ambient temperature, and these were found to randomly impact the absolute values of grain diameter. To enable simple comparison between the various series in Figure 2, we thus plot the average correlation length normalized to its maximum value in a given series. Absolute values of this maximum diameter
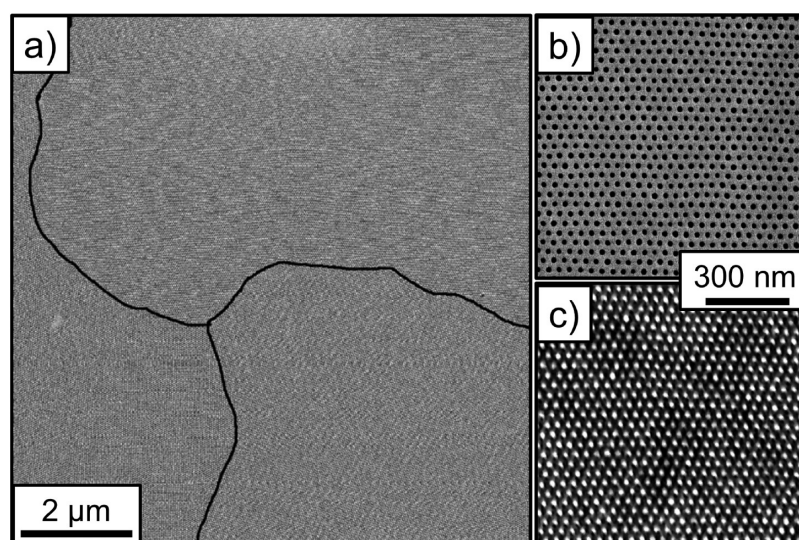
Figure 3. Scanning electron micrographs for optimally annealed (Φ_{THF} = 0.55, 3 min) SL (43-20) films post PLA degradation and coating with 3 nm of Pt. (a) Large-scale image (10×10 μm^2) showing long correlation lengths, based on the clear Moiré pattern. The solid black lines are a guide to the eye illustrating the grain boundaries. (b) 1×1 μm^2 magnified view from a region shown in (a). (c) High magnification image of a Ni nanodot pattern (1×1 μm^2) resulting from a Damascene-like lithography process[10] using a degraded SL (43-20) film as a template.

varied between 1.1 and 6.9 μm, with an average of 3 μm over all experiments.

Four distinct investigations are summarized in Figure 2. The first focuses on the thickness dependence (Figure 2a) of SVA of the SL (51-24) polymer, including films with thickness 60, 120, and 300 nm, annealed at pressures below 1 psig. A well-defined peak is observed in the range $0.55 \leq \Phi_{THF} \leq 0.57$ for both 60 and 120 nm films, consistent with the illustrative data presented in Figure 1. In contrast, the correlation length increases monotonically with Φ_{THF} for 300 nm thickness. For $\Phi_{THF} >$ 0.6, films were destroyed via dewetting or THF condensation, limiting the range of this study. The second investigation (Figure 2b−e) probes the dependence on molar mass and PLA volume fraction for four different polymers (SL (43-20), SL (51-24), SL (73-24), and SL (79-24)), with f_{PLA} = 0.28, 0.28, 0.23, and 0.21, respectively. The behavior is qualitatively similar for all BCPs. Specifically, in each case a peak in the correlation length is observed at $0.55 \leq \Phi_{THF} \leq 0.57$ for low pressure SVA, while a monotonic increase with Φ_{THF} is observed for high pressure SVA. The third investigation probes the effect of BCP synthesis method and dispersion in molar mass on SVA. Results obtained with synthesis method 1 (see Methods), resulting in a significantly lower dispersion in molar mass, are shown in Figure 2b. These data can be compared to those shown in Figure 2c−e, which result from the use of synthesis method 2 (see Methods). The behavior is essentially identical between the two synthesis methods. Most significantly, Figure 2b and c, for polymers with similar f_{PLA}, exhibit qualitatively similar behavior for both high and low pressure SVA. The only difference in fact, which is not captured in Figure 2, is the absolute grain size observed for SL (43-20), which was consistently larger than the other polymers studied. Specifically, the peak grain diameter for SL (43-20) was 6.9 ± 0.8 μm, whereas the remaining BCPs had peak diameters ranging from 1.1 to 3 μm. The final investigation focuses on the influence of vapor pressure during SVA, which can be independently controlled at constant Φ_{THF}. As can be seen from Figure 2b−e, the observed high pressure (>10 psig) behavior is significantly different from that at low pressure (<1 psig). In all cases, low

pressure anneals resulted in a well-defined peak in correlation length with consistently larger maximum absolute grain sizes (on average, 2.3 times larger). High pressure anneals, however, resulted in a monotonic increase in correlation length with Φ_{THF}, up to the point where dewetting occurred. Of note, the low and high pressure SVA behaviors mimic quite closely the differences seen between thinner (60, 120 nm) and thicker (300 nm) films.

Representative SEM images for the SL (43-20) film exposed to Φ_{THF} = 0.55 (Figure 2b) are shown in Figure 3. In the large-scale image (10×10 μm^2, Figure 3a), the intersection of three grains is shown, the black lines marking the grain boundaries. In such cases, where the correlation lengths are so large that the required low magnifications preclude direct observation of the pores, exact determination of the grain size was still possible via the clearly visible Moiré pattern.[45] In this case, grain boundaries could easily be identified by abrupt changes in this pattern, and analysis of smaller regions (e.g., Figure 3b) confirmed the accuracy of this method to locate grain boundaries and determine correlation lengths. High magnification images (e.g., 1×1 μm^2, Figure 3b) reveal essentially defect-free hexagonally close packed ordering with center-to-center spacing of 38.0 ± 0.6 nm and feature diameter of 19.8 ± 0.8 nm.

The BCP template shown in Figure 3a,b was used for Ni nanodot formation via the Damascene nanolithographic process we reported earlier,[10] providing a stringent test of template quality. The resultant nanodot array (Figure 3c), obtained by brief oxygen plasma etching of the BCP film followed by Ni evaporation and Ar milling (see Methods), exhibits essentially defect-free, long-range order, much like the parent template, with a center-to-center spacing of 38.2 ± 0.7 nm and a nanodot diameter of 19.1 ± 0.8 nm.

We also performed two additional microscopy investigations to probe the detailed structure of the cylindrical pores. In the first, the film shown in Figure 3a,b was O_2 plasma etched (to remove any wetting and HMDS adhesion layers,[10] see Methods) and immersed in liquid N_2. A section of the polymer film could then be removed with a sharp blade, thus exposing a cross-section, which was imaged by SEM at a tilt angle of ~30°

above the substrate surface. Figure 4a clearly shows pores that run perpendicular to the film surface and extend through the
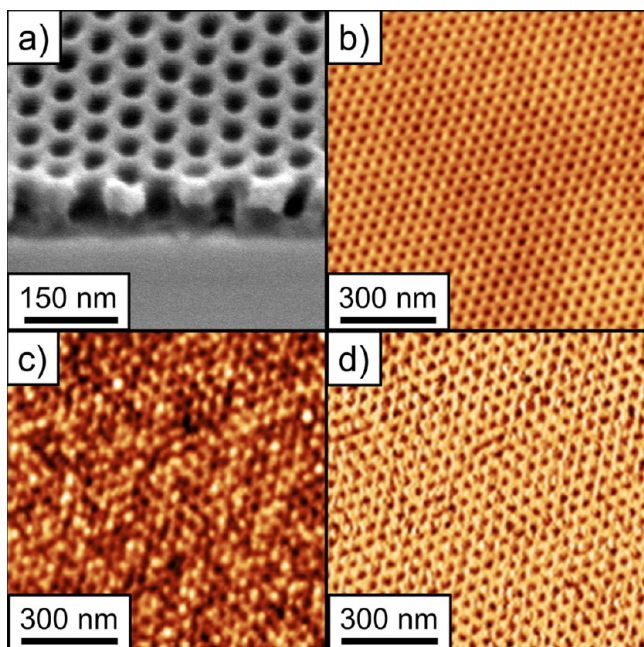

Figure 4. Pores span the entire thickness of an optimally annealed (Φ_{THF} = 0.55, 3 min) 60 nm SL (43-20) film post PLA degradation and a brief O_2 reactive ion etch. (a) 500 × 500 nm^2 SEM micrograph near a scratch in the PS-PLA film at a tilt angle of ~30° above the horizontal. Pores at the scratch are nominally perpendicular to the substrate surface and clearly span the entire thickness. (b) 1 × 1 μm^2 tapping-mode AFM image of the top surface of the film. (c,d) 1 × 1 μm^2 tapping-mode AFM images of the bottom surface of the film, where (c) presents the tip height and (d) the phase (shown here to improve contrast). The hexagonal pattern of pores persists from the top surface (b) to the bottom surface (c,d). AFM height scale is 20 nm.

bulk of the film to the substrate surface. In the second test, polymer films cooled to liquid N_2 temperatures were stripped from the Si substrate with double-sided adhesive tape, and their "back-side" (formerly the polymer/substrate interface) was imaged using AFM. Figure 4b first shows an AFM image of the top surface, reproducing the highly ordered hexagonal porous structure seen in the SEM images of Figure 3. Figure 4c is a tapping-mode AFM height image of the back-side of the BCP film. The accompanying phase image in Figure 4d, which introduces contrast due to variation in mechanical properties, again clearly evidences a hexagonal array of pores at what was originally the polymer film/substrate interface.

B. Small-Angle X-ray Scattering on Bulk Polymers. We have shown that for BCP film thicknesses of 120 nm and below, in all four PS-PLA samples studied, optimized templates were obtained in a relatively narrow Φ_{THF} window, centered around 0.55. To further understand the origin of this window, and to better understand the solvent-swollen state of the BCP films, we performed comparative SAXS experiments on bulk PS-PLA specimens solvent-loaded to similar Φ_{THF} values. PS-PLA samples were loaded into preweighed Al differential scanning calorimetry (DSC) "pans", and the mass of the polymer was determined (~10s of mg). Solvent was subsequently added using a micropipette, the volume being determined from measurements of the mass after sealing the pans with a

preweighed cap. On the basis of their sealed mass, specimens with Φ_{THF} values of 0.40, 0.60, 0.63, 0.65, 0.68, and 0.70 were produced. The mass of the sealed pan was periodically checked and never varied by more than 0.5% over months, indicating a high integrity seal. Using such samples, SAXS data were then recorded at room temperature as a function of Φ_{THF}.

Example data (SAXS scattering intensity, I, vs magnitude of the scattering wavevector, q) are shown in Figure 5 for SL (51-24) at various Φ_{THF} from 0 to 0.70. At $\Phi_{THF} \leq 0.60$, microphase separation into a hexagonally ordered array of cylinders is obvious, the principal scattering peak (labeled with an asterisk) being followed by additional higher order peaks at relative positions of $\sqrt{3}:2:\sqrt{7}:3$. In the range $0.60 < \Phi_{THF} \leq 0.68$, however, the higher order reflections are diminished, and
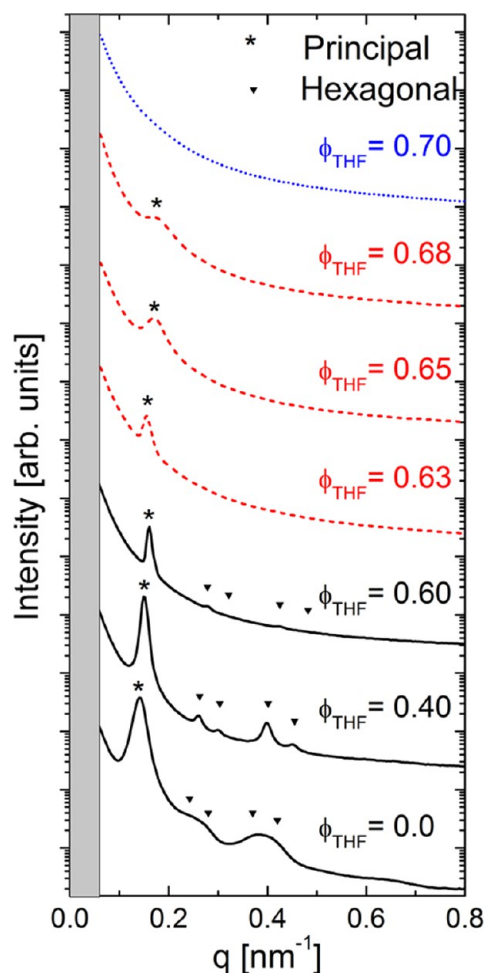

Figure 5. SAXS intensity versus scattering vector, q, for SL (51-24) obtained at 298 K. Data were obtained with the polymers hermetically sealed in a DSC pan with various Φ_{THF}. Triangles (▼) indicate scattering peaks associated with a hexagonal close-packed cylindrical morphology, based upon the principal reflection (*). Black solid lines have well-defined peaks associated with the hexagonal morphology. Blue dotted lines show no indication of any scattering peaks associated with microphase separation (i.e., they are disordered and nominally homogeneous). Red dashed curves represent the order/disorder transition region, where a principal scattering peak indicates short-range order, but the significant increase in the full width at half-maximum, and absence of secondary peaks, indicates a lack of long-range order as described further in Figure 6 and in the text. These data were previously published in ref 46 that focused on the microrheology of THF swollen PS-PLA thin films.

the principal scattering peak broadens. At $\Phi_{THF} > 0.68$, no scattering peaks were observed. The evolution of the important SAXS parameters with Φ_{THF} is summarized in Figure 6, where
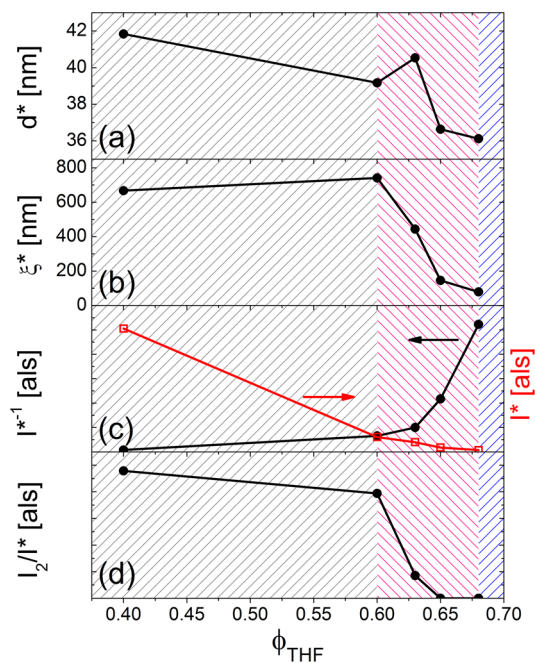

Figure 6. Summary of the Lorentz-corrected SAXS peak parameters for SL (51-24) versus volume concentration of THF (Φ_{THF}). (a) Principal domain spacing d^*. (b) Correlation length ξ^*. (c) The intensity of the principal scattering peak I^* (with background Porod scattering subtracted; see Supporting Information Figure S1), ●, and its reciprocal I^{*-1}, red □. (d) The ratio of the $\sqrt{3}q^*$ peak intensity (I_2) to the principal scattering peak intensity I^* (with background Porod scattering subtracted; see Supporting Information Figure S1). The three shaded regions correspond to the three regions in Figure 5: black, well-defined peaks with hexagonal morphology; red, order/disorder transition region; blue, disordered/homogeneous.

we plot the Φ_{THF} dependence of the principal domain spacing ($d^* = 2\pi/q^*$), the correlation length ($\xi^* = 2\pi/\sigma^*$, where σ^* is the width of the principal scattering peak), the principal scattering peak intensity and its reciprocal (I^* and I^{*-1}), and the ratio of intensities between the $\sqrt{3}q^*$ peak, and the principal peak intensity (I_2/I^*). Although instrumental broadening was not included in this calculation, the highest extracted values for ξ^* are not resolution limited (see Methods). As illustrated in detail in Supporting Information Figure S1, Lorentz and background Porod contributions (and a constant background) were subtracted from the data prior to fitting with Lorentzian peaks to extract the above parameters.

We interpret the three regimes in Figures 5 and 6 in terms of an evolution with Φ_{THF} from an ordered state (up to $\Phi_{THF} = 0.60$), through a state close to the ODT ($0.60 < \Phi_{THF} \leq 0.68$), to a clearly disordered/nominally homogeneous state ($\Phi_{THF} > 0.68$). The transitions between these regimes are clear from each of the parameters plotted in Figure 6a–d. For instance, d^* (Figure 6a) initially decreases with increasing Φ_{THF}, as expected, before exhibiting a clear anomaly around $\Phi_{THF} = 0.60-0.63$, likely marking the ODT anticipated to occur in this region, or a morphology change (i.e., to spheres). Similarly, ξ^* (Figure 6b) changes only minimally up to $\Phi_{THF} = 0.60$ (where it takes values of 670–740 nm, consistent with long-range order), at which point a dramatic decrease occurs, leveling off

around 100 nm at $\Phi_{THF} = 0.68$. This decrease derives from the loss of long-range order as the ODT is approached. The corresponding loss of intensity in the principal scattering peak (Figure 6c) is perhaps best seen from the I^{*-1} plot (left axis), which reveals a distinct upturn starting around $\Phi_{THF} = 0.60$ (the expected decrease in I^* with Φ_{THF} due to dilution is also depicted in Figure 6c). We also observe an accompanying decrease in I_2/I^*, where I_2 is the $\sqrt{3}q^*$ peak intensity, at $\Phi_{THF} = 0.60$, this ratio approaching zero by $\Phi_{THF} = 0.65$, again consistent with the loss of long-range order above $\Phi_{THF} = 0.60$. Note that in the literature on temperature-driven ODTs in neat BCPs, issues such as critical behavior, the extent to which the transition is first order, and the manner in which the higher order peaks vanish through the ODT (which probes how the Fourier components of the chemical modulation vanish) have been considered in detail.[47] In our case, the much lower density of data points in the critical region precludes this.

The most important point to take away from these experiments is that the region in which our thin film SVA studies reveal a clear optimization of lateral ordering (i.e., $\Phi_{THF} = 0.54-0.57$) clearly lies on the ordered side of the ODT determined from these comparative SAXS studies (i.e., $\Phi_{THF} \approx 0.60$). Assuming that the ODT in our films occurs at Φ_{THF} similar to the identical bulk polymers we studied with SAXS (i.e., assuming that finite size, surface effects, and related issues do not induce large shifts in the ODT in these solvent swollen films, as recently shown for symmetric poly(styrene-*block*-[isoprene-*ran*-epoxyisoprene]) thin films[48]), we are led to the conclusion that the optimal Φ_{THF} for SVA lies just on the ordered side of the ODT. Similar SAXS measurements on bulk versions of the other three polymers studied (i.e., the ones shown in Figure 2) corroborate the generality of this conclusion. In each case, the data recorded were quantitatively similar to those shown in Figure 5, the ODT occurring in a similar region of Φ_{THF}. This is summarized in the phase diagram of Supporting Information Figure S5 in the $\Phi_{THF}-f_{PLA}$ plane, the ODT region lying between $\Phi_{THF} = 0.60$ and 0.70 in each case. Comparing to Figure 2, we find, quite generally for cylinder-forming PS-PLA BCPs, that the optimum window of Φ_{THF} for achieving highly ordered thin films post SVA lies close to but just on the ordered side of the ODT determined from comparative SAXS studies in bulk.

■ DISCUSSION

We posit that our collective SVA results can be qualitatively understood by analogy to thermal annealing of other single-component solids such as bulk polycrystalline elemental metals formed from the melt. In such systems, the grain size is typically optimized by annealing just below the melting point (i.e., on the ordered side of the transition), where the diffusion-controlled and thermally activated processes required for recrystallization and grain growth are optimally fast. In contrast, annealing above the melting point (i.e., on the disordered side of the transition) followed by a fast quench results in much smaller grain size. By analogy, we propose that our observed optimal window of Φ_{THF} for SVA of BCP thin films lies just on the ordered side of the ODT, where the thermally activated processes required for increase of the lateral correlation length are maximized. Furthermore, as illustrated in Figure 1c, the grain growth is apparently quite rapid (<1 s of steady-state solvent exposure) after initial nucleation under such conditions. Under the quench conditions used in this work, however, increasing Φ_{THF} beyond the ODT (i.e., into the disordered
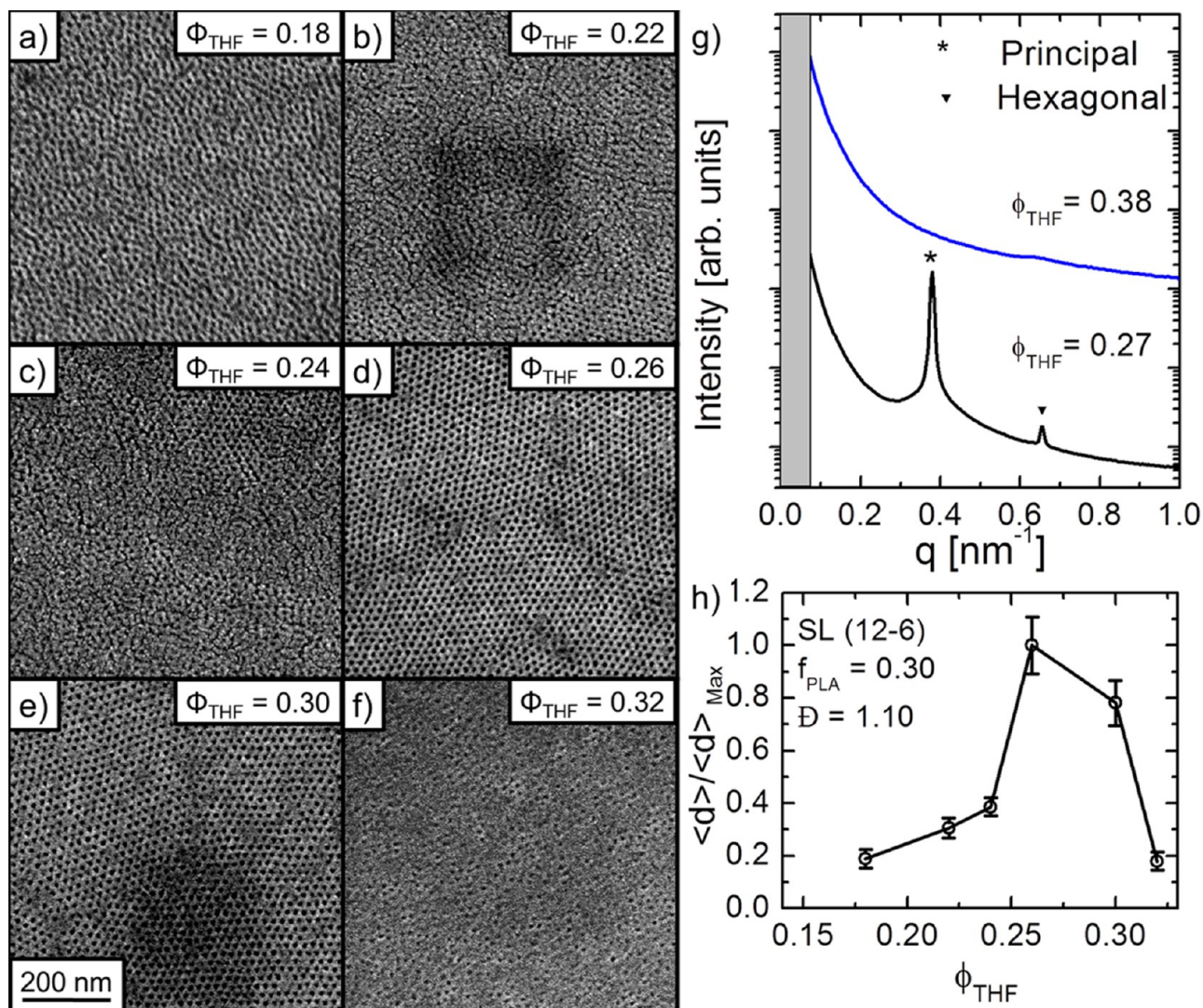
Figure 7. Small-angle X-ray scattering data are used to predict the ideal solvent concentration to yield large correlation lengths for a low molecular weight PS-PLA BCP (M_n = 18 kg mol^{-1}), with a center-to-center spacing of only 18 nm. Representative scanning electron micrograph images (a−f) for 60 nm thick SL (12-6) films, after PLA degradation and 3 nm Pt sputter coating, as a function of THF concentration exposure (Φ_{THF}) near the order/disorder transition defined by bulk SAXS measurements (g). Each image is 1 × 1 μm^2. Films were exposed to the designated solvent concentration for 3 min and "quenched" in less than 1 s. Grain size analysis (h) shows a peak in the average grain diameter. Error bars represent the standard deviation of multiple trials.

state) leads to the ultimate formation of a much less ordered structure (e.g., Figure 1e,f), longer anneal times being ineffective. At the other extreme, low Φ_{THF} values during SVA result in little change from the original, kinetically trapped, morphology in the as-cast state (e.g., Figure 1a). In this regime, longer solvent exposure times could potentially lead to improved organization, although this was not pursued here.

In consideration of drying time, there are essentially four variables that can be varied to control the rate of solvent evaporation in our SAC: (i) chamber pressure, (ii) initial film thickness, (iii) swollen film thickness, and (iv) the SAC purge gas flow rate. The first three were systematically investigated. Because of the finite impedance of the SAC outlet (Supporting Information Figure S2-B), the quench rate decreases with increasing SVA pressure, as verified by high frequency thickness measurements. Similar observations confirmed that thinner films experience a more rapid quench, as expected. The film thickness in the swollen state also affects the quench rate, higher thicknesses (and therefore higher Φ_{THF}) resulting in

lower quench rates. Finally, the quench rate increases with increased purge gas flow rate. With these factors appreciated, many of the observations from Figure 2 can be better understood. For instance, fast quenching (i.e., in less than 1 s), whether favored by low SVA pressure or low film thickness, consistently yields a peak in correlation length at $\Phi_{THF} \approx 0.55$ (see Figure 2). Films annealed under these conditions further exhibit low defect densities and perpendicularly oriented pores that traverse the entire film thickness, consistent with recent theory on ordering kinetics in PS-PLA.[18,49] When Φ_{THF} exceeds this optimal window, however, rapid quenching results in disordered, mixed phase structures due to insufficient time for appreciable grain growth as crystallization occurs.

Slow quenching (i.e., in greater than 3 s, with an average of 5 s), whether driven by high SVA pressure or large film thickness, provides very different results, often less reproducible. As seen from Figure 2, for instance, slower quenching, as a result of the use of thicker films or higher pressures, leads to a monotonic increase in correlation length with Φ_{THF} up to the point of

delamination/dewetting. While correlation lengths do increase, it is important to emphasize that thick films were observed to have well-ordered pores only at the free surface (as shown in Figure 2), not traversing the whole thickness of the film. Observations of the film/substrate interface in fact displayed a mixed (often predominantly in-plane) state with little lateral ordering and a low level of reproducibility. We ascribe this to the depthwise solvent concentration gradients expected to occur over the significant period of time required for slower solvent removal rates. Such a situation leads to small regions of ordering in orientations largely controlled by the local evaporation rate,[18] thickness (due to commensurability issues), solvent vapor purity (e.g., the presence of water vapor, for example), or other poorly controlled factors. Such ambiguities no doubt contribute to the observed wide variety of final film morphologies obtained for similar SVA parameters, as seen in the literature.[10,39]

Finally, to demonstrate the generality of our results, we tested the predictive power of our form of SAXS analysis in optimizing thin film PS-PLA templates through the use of a low molar mass PS-PLA BCP synthesized using method 2 (see Methods), designated SL (12-6), with M_n = 18 kg/mol and f_{PLA} = 0.30. SAXS measurements were performed on neat bulk samples, confirming hexagonally close-packed cylinders, with an 18 nm center-to-center spacing. Thus, as expected, the much lower molar mass leads to significantly smaller feature size, an attractive regime for lithographic applications. SAXS measurements were then made as a coarse function of Φ_{THF}, seeking simply to determine the approximate ODT concentration. As shown in Figure 7g, this was determined to lie in the approximate range $0.27 < \Phi_{THF} < 0.38$. On the basis of this, and the conclusions drawn above, 60 nm thick films were then solvent annealed for 3 min under low pressure (1 psig), high quench rate conditions (<1 s), from Φ_{THF} = 0.18 to 0.32, that is, in a Φ_{THF} range roughly centered on a region encompassing the ordered side of the anticipated ODT of $\Phi_{THF} < 0.38$. Representative SEM images are shown in Figure 7a–f, and the extracted lateral correlation lengths are plotted in Figure 7h. Just as expected, a well-defined peak in grain size occurs around $0.26 < \Phi_{THF} < 0.30$, where the films exhibit perpendicular cylinder alignment, grain diameters of 212 ± 24 nm (reduction in absolute grain size, cf., higher molar mass BCPs, is not likely due to T_g effects, see Methods), and low defect density. At lower Φ_{THF} values, the morphology is similar to the as-cast case, whereas at higher Φ_{THF}, the films have a mixed morphology that even exhibits some PS capping at the surface. The results are thus consistent with expectations based on the conclusions reached above.

SUMMARY AND CONCLUSIONS

By combining controlled solvent vapor annealing experiments with in situ thickness monitoring, we have identified optimal parameters for SVA of cylinder-forming PS-PLA BCP thin films. Films with hexagonally close-packed perpendicularly aligned cylinders traversing the entire thickness of the film, low defect densities, and large lateral correlation lengths were achieved at short annealing times. Average grain diameters of 6.9 ± 0.8 μm were attained in SL (43-20), with single grains approaching 10 μm across. These general results were achieved regardless of the molecular synthesis method employed, the BCP molar mass, and the BCP composition. Importantly, such patterns were then transferred to a magnetic metal with high fidelity. In our studies, a narrow window of solvent

concentration in the film during SVA gave the highest correlation lengths and lowest defect densities. Comparative SAXS data on solvated PS-PLA samples of identical composition revealed that this window lies just on the ordered side of the ODT in all samples measured, an observation we interpret by analogy with thermal annealing of other single component systems. Moreover, fast evaporation (favored by low film thickness, low solvent annealing pressures, and large purge gas flow rates) yielded consistent and reproducible results. Conversely, slow evaporation rates at the end of the annealing process resulted in varied degrees of ordering, variable film morphologies, an inability of the minority phase cylinders to traverse the entire film thickness, and significant irreproducibility. The generality of our results was demonstrated via similar work on a much lower molar mass BCP, generating highly organized templates with cylinder diameters down to 10 nm (center-to-center spacing of 18 nm). We believe that these conclusions have important implications for the solvent vapor annealing of BCPs used for a number of nanotemplating and membrane applications. In particular, the general analogy to thermal annealing of other single component systems (i.e., annealing just on the ordered side of the ODT) implies that an optimized window for solvent concentration in solvent vapor annealing may well be generalizable to other BCP systems, based solely on the solvent concentration associated with the onset of disorder.

■ ASSOCIATED CONTENT

ⓈSupporting Information

S1: Fitting of Lorentz-corrected SAXS data for six THF concentrations, including the cylindrical phase, the order/disorder transition, and the disordered phase. S2: Three-dimensional illustration of the solvent vapor annealing chamber. S3: Representative solvent concentration, Φ_{THF}, versus time profile, as measured by the spectral reflectance determined film thickness. S4: Representative SEM image analysis steps and corresponding discussion. S5: "Phase diagram" of bulk morphology, observed by SAXS, as a function of volume fraction of THF (Φ_{THF}) and volume fraction of PLA (f_{PLA}), where total molar mass ranged from 75−103 kg/mol. This material is available free of charge via the Internet at http://pubs.acs.org.

■ AUTHOR INFORMATION

Corresponding Authors
*E-mail: hillmyer@umn.edu.
*E-mail: leighton@umn.edu.
Present Addresses
[†]Department of Physics, Creighton University, Omaha, Nebraska 68178, United States.
[‡]Graduate School of Nanoscience and Technology, KAIST, Daejeon 305-701, Korea.
Notes
The authors declare no competing financial interest.

■ ACKNOWLEDGMENTS

■ REFERENCES

(1) Bang, J.; Jeong, U.; Ryu, D. Block Copolymer Nanolithography: Translation of Molecular Level Control to Nanoscale Patterns. *Adv. Mater.* **2009**, *21*, 4769−4792.

(2) Park, S.; Lee, D. H.; Xu, J.; Kim, B.; Hong, S. W.; Jeong, U.; Xu, T.; Russell, T. P. Macroscopic 10-Terabit-per-Square-Inch Arrays from Block Copolymers with Lateral Order. *Science* **2009**, *323*, 1030−1033.

(3) Hamley, I. Ordering in Thin Films of Block Copolymers: Fundamentals to Potential Applications. *Prog. Polym. Sci.* **2009**, *34*, 1161−1210.

(4) Lazzari, M.; López-Quintela, M. A. Block Copolymers as a Tool for Nanomaterial Fabrication. *Adv. Mater.* **2003**, *15*, 1583−1594.

(5) Cheng, J.; Ross, C.; Chan, V. Formation of a Cobalt Magnetic Dot Array via Block Copolymer Lithography. *Adv. Mater.* **2001**, 1174−1178.

(6) Thurn-Albrecht, T.; Steiner, R.; DeRouchey, J.; Stafford, C. M.; Huang, E.; Bal, M.; Tuominen, M.; Hawker, C. J.; Russell, T. P. Nanoscopic Templates from Oriented Block Copolymer Films. *Adv. Mater.* **2000**, *12*, 787−791.

(7) Ruiz, R.; Kang, H.; Detcheverry, F. A.; Dobisz, E.; Kercher, D. S.; Albrecht, T. R.; Pablo, J. J. de; Nealey, P. F. Density Multiplication and Improved Lithography by Directed Block Copolymer Assembly. *Science* **2008**, *321*, 936−939.

(8) Park, S.; Wang, J.-Y.; Kim, B.; Xu, J.; Russell, T. P. A Simple Route to Highly Oriented and Ordered Nanoporous Block Copolymer Templates. *ACS Nano* **2008**, *2*, 766−772.

(9) Bates, C. M.; Maher, M. J.; Janes, D. W.; Ellison, C. J.; Willson, C. G. Block Copolymer Lithography. *Macromolecules* **2014**, *47*, 2−22.

(10) Baruth, A.; Rodwogin, M. D.; Shankar, A.; Erickson, M. J.; Hillmyer, M. A.; Leighton, C. Non-Lift-off Block Copolymer Lithography of 25 Nm Magnetic Nanodot Arrays. *ACS Appl. Mater. Interfaces* **2011**, *3*, 3472−81.

(11) Xiao, S.; Yang, X.; Edwards, E. W.; La, Y.-H.; Nealey, P. F. Graphoepitaxy of Cylinder-Forming Block Copolymers for Use as Templates to Pattern Magnetic Metal Dot Arrays. *Nanotechnology* **2005**, *16*, S324−S329.

(12) Son, J. G.; Chang, J.-B.; Berggren, K. K.; Ross, C. A. Assembly of Sub-10-Nm Block Copolymer Patterns with Mixed Morphology and Period Using Electron Irradiation and Solvent Annealing. *Nano Lett.* **2011**, *11*, 5079−5084.

(13) Bates, F. S. Polymer-Polymer Phase Behavior. *Science* **1991**, *251*, 898−905.

(14) Kim, S. H.; Misner, M. J.; Xu, T.; Kimura, M.; Russell, T. P. Highly Oriented and Ordered Arrays from Block Copolymers via Solvent Evaporation. *Adv. Mater.* **2004**, *16*, 226−231.

(15) Knoll, A.; Horvat, A.; Lyakhova, K. Phase Behavior in Thin Films of Cylinder-Forming Block Copolymers. *Phys. Rev. Lett.* **2002**, *89*, 035501.

(16) Kubo, T.; Wang, R. F.; Olson, D. A.; Rodwogin, M.; Hillmyer, M. A.; Leighton, C. Spontaneous Alignment of Self-Assembled ABC

(17) Gowd, E. B.; Böhme, M.; Stamm, M. In Situ GISAXS Study on Solvent Vapour Induced Orientation Switching in PS- b -P4VP Block Copolymer Thin Films. *IOP Conf. Ser. Mater. Sci. Eng.* **2010**, *14*, 012015.

(18) Phillip, W.; Hillmyer, M.; Cussler, E. Cylinder Orientation Mechanism in Block Copolymer Thin Films upon Solvent Evaporation. *Macromolecules* **2010**, *43*, 7763−7770.

(19) Mansky, P.; Russell, T.; Hawker, C.; Mays, J.; Cook, D.; Satija, S. Interfacial Segregation in Disordered Block Copolymers: Effect of Tunable Surface Potentials. *Phys. Rev. Lett.* **1997**, *79*, 237−240.

(20) Han, E.; Stuen, K. O.; Leolukman, M.; Liu, C.-C.; Nealey, P. F.; Gopalan, P. Perpendicular Orientation of Domains in Cylinder-Forming Block Copolymer Thick Films by Controlled Interfacial Interactions. *Macromolecules* **2009**, *42*, 4896−4901.

(21) Sinturel, C.; Vayer, M.; Morris, M.; Hillmyer, M. A. Solvent Vapor Annealing of Block Polymer Thin Films. *Macromolecules* **2013**, *46*, 5399−5415.

(22) Kelly, J. Y.; Albert, J. N. L.; Howarter, J. A.; Kang, S.; Stafford, C. M.; Epps, T. H.; Fasolka, M. J. Investigation of Thermally Responsive Block Copolymer Thin Film Morphologies Using Gradients. *ACS Appl. Mater. Interfaces* **2010**, *2*, 3241−3248.

(23) Di, Z.; Posselt, D.; Smilgies, D.-M.; Papadakis, C. M. Structural Rearrangements in a Lamellar Diblock Copolymer Thin Film during Treatment with Saturated Solvent Vapor. *Macromolecules* **2010**, *43*, 418−427.

(24) Sun, Y.; Henderson, K. J.; Jiang, Z.; Strzalka, J. W.; Wang, J.; Shull, K. R. Effects of Reactive Annealing on the Structure of Poly(methacrylic acid)−Poly(methyl Methacrylate) Diblock Copolymer Thin Films. *Macromolecules* **2011**, *44*, 6525−6531.

(25) Nandan, B.; Vyas, M. K.; Böhme, M.; Stamm, M. Composition-Dependent Morphological Transitions and Pathways in Switching of Fine Structure in Thin Films of Block Copolymer Supramolecular Assemblies. *Macromolecules* **2010**, *43*, 2463−2473.

(26) Lodge, T. P.; Pudil, B.; Hanley, K. J. The Full Phase Behavior for Block Copolymers in Solvents of Varying Selectivity. *Macromolecules* **2002**, *35*, 4707−4717.

(27) Hui, C.-Y.; Wu, K.-C.; Lasky, R. C.; Kramer, E. J. Case-II Diffusion in Polymers. I. Transient Swelling. *J. Appl. Phys.* **1987**, *61*, 5129.

(28) Hui, C.-Y.; Wu, K.-C.; Lasky, R. C.; Kramer, E. J. Case-II Diffusion in Polymers. II. Steady-State Front Motion. *J. Appl. Phys.* **1987**, *61*, 5137.

(29) Shibayama, M.; Hashimoto, T.; Hasegawa, H.; Kawai, H. Ordered Structure in Block Polymer Solutions. 3. Concentration Dependence of Microdomains in Nonselective Solvents. *Macromolecules* **1983**, *16*, 1427−1433.

(30) Son, J. G.; Gotrik, K. W.; Ross, C. A. High-Aspect-Ratio Perpendicular Orientation of PS- b -PDMS Thin Films under Solvent Annealing. *ACS Macro Lett.* **2012**, *1*, 1279−1284.

(31) Jung, Y. Y. S.; Ross, C. A. Solvent Vapor Induced Tunability of Self Assembled Block Copolymer Patterns. *Adv. Mater.* **2009**, *21*, 2540−2545.

(32) Albert, J. N. L.; Young, W.-S.; Lewis, R. L.; Bogart, T. D.; Smith, J. R.; Epps, T. H. Systematic Study on the Effect of Solvent Removal Rate on the Morphology of Solvent Vapor Annealed ABA Triblock Copolymer Thin Films. *ACS Nano* **2012**, *6*, 459−466.

(33) Fredrickson, G. H.; Bates, F. S. Dynamics of Block Copolymers: Theory and Experiment. *Annu. Rev. Mater. Sci.* **1996**, *26*, 501−550.

(34) Bosworth, J. K.; Paik, M. Y.; Ruiz, R.; Schwartz, E. L.; Huang, J. Q.; Ko, A. W.; Smilgies, D.-M.; Black, C. T.; Ober, C. K. Control of Self-Assembly of Lithographically Patternable Block Copolymer Films. *ACS Nano* **2008**, *2*, 1396−1402.

(35) Gu, X.; Gunkel, I.; Hexemer, A.; Gu, W.; Russell, T. P. An in Situ Grazing Incidence X-Ray Scattering Study of Block Copolymer Thin Films During Solvent Vapor Annealing. *Adv. Mater.* **2014**, *26*, 273−281.

Triblock Terpolymers for Large-Area Nanolithography. *Appl. Phys. Lett.* **2008**, *93*, 133112.

(36) Cavicchi, K. A.; Russell, T. P. Solvent Annealed Thin Films of Asymmetric Polyisoprene−Polylactide Diblock Copolymers. *Macromolecules* **2007**, *40*, 1181−1186.

(37) Paradiso, S. P.; Delaney, K. T.; García-Cervera, C. J.; Ceniceros, H. D.; Fredrickson, G. H. Block Copolymer Self Assembly during Rapid Solvent Evaporation: Insights into Cylinder Growth and Stability. *ACS Macro Lett.* **2014**, *3*, 16−20.

(38) Huang, E.; Mansky, P.; Russell, T. P.; Harrison, C.; Chaikin, P. M.; Register, R. A.; Hawker, C. J.; Mays, J. Mixed Lamellar Films: Evolution, Commensurability Effects, and Preferential Defect Formation. *Macromolecules* **2000**, *33*, 80−88.

(39) Vayer, M.; Hillmyer, M. A.; Dirany, M.; Thevenin, G.; Erre, R.; Sinturel, C. Perpendicular Orientation of Cylindrical Domains Upon Solvent Annealing Thin Films of Polystyrene-b-Polylactide. *Thin Solid Films* **2010**, *518*, 3710−3715.

(40) Bang, J.; Kim, B. J.; Stein, G. E.; Russell, T. P.; Li, X.; Wang, J.; Kramer, E. J.; Hawker, C. J. Effect of Humidity on the Ordering of PEO-Based Copolymer Thin Films. *Macromolecules* **2007**, *40*, 7019−7025.

(41) Tang, C.; Bang, J.; E. Stein, G.; Fredrickson, G. H.; Hawker, C. J.; Kramer, E. J.; Sprung, M.; Wang, J. Square Packing and Structural Arrangement of ABC Triblock Copolymer Spheres in Thin Films. *Macromolecules* **2008**, *41*, 4328−4339.

(42) Olayo-Valles, R.; Lund, M. S.; Leighton, C.; Hillmyer, M. A. Large Area Nanolithographic Templates by Selective Etching of Chemically Stained Block Copolymer Thin Films. *J. Mater. Chem.* **2004**, *14*, 2729.

(43) Cser, F. About the Lorentz Correction Used in the Interpretation of Small Angle X-Ray Scattering Data of Semicrystalline Polymers. *J. Appl. Polym. Sci.* **2001**, *80*, 2300−2308.

(44) Crossland, E. J. W.; Cunha, P.; Ludwigs, S.; Hillmyer, M. A.; Steiner, U. In Situ Electrochemical Monitoring of Selective Etching in Ordered Mesoporous Block-Copolymer Templates. *ACS Appl. Mater. Interfaces* **2011**, *3*, 1375−9.

(45) Read, D. R.; Dally, J. W. Theory of Electron Beam Moire. *J. Res. Natl. Inst. Stand. Technol.* **1996**, *101*, 47.

(46) Kim, J. C.; Seo, M.; Hillmyer, M. A.; Francis, L. F. Magnetic Microrheology of Block Copolymer Solutions. *ACS Appl. Mater. Interfaces* **2013**, *5*, 11877−11883.

(47) Sakamoto, N.; Hashimoto, T. Order-Disorder Transition of Low Molecular Weight Polystyrene-Block-Polyisoprene. 1. SAXS Analysis of Two Characteristic Temperatures. *Macromolecules* **1995**, *28*, 6825−6834.

(48) Kim, S.; Nealey, P. F.; Bates, F. S. Directed Assembly of Lamellae Forming Block Copolymer Thin Films near the Order-Disorder Transition. *Nano Lett.* **2013**, *14*, 12−16.

(49) Goveas, J. L.; Milner, S. T. Dynamics of the Lamellar−Cylindrical Transition in Weakly Segregated Diblock Copolymer Melts. *Macromolecules* **1997**, *30*, 2605−2612.